

Revealing emergent many-body phenomena by analyzing large-scale space-time records of monitored quantum systems

Marcel Cech,¹ Cecilia De Fazio,¹ María Cea,^{2,3} Mari Carmen Bañuls,^{2,3} Igor Lesanovsky,^{1,4} and Federico Carollo⁵

¹*Institut für Theoretische Physik and Center for Integrated Quantum Science and Technology, Universität Tübingen, Auf der Morgenstelle 14, 72076 Tübingen, Germany*

²*Max-Planck-Institut für Quantenoptik, Hans-Kopfermann-Str. 1, D-85748 Garching, Germany*

³*Munich Center for Quantum Science and Technology (MCQST), Schellingstr. 4, D-80799 München, Germany*

⁴*School of Physics and Astronomy and Centre for the Mathematics and Theoretical Physics of Quantum Non-Equilibrium Systems,*

The University of Nottingham, Nottingham, NG7 2RD, United Kingdom

⁵*Centre for Fluid and Complex Systems, Coventry University, Coventry, CV1 2TT, United Kingdom*

Recent advances in quantum simulators permit unitary evolution interspersed with locally resolved mid-circuit measurements. This paves the way for the observation of large-scale space-time structures in quantum trajectories and opens a window for the *in situ* analysis of complex dynamical processes. We demonstrate this idea using a paradigmatic dissipative spin model, which can be implemented, e.g., on Rydberg quantum simulators. Here, already the trajectories of individual experimental runs reveal surprisingly complex statistical phenomena. In particular, we exploit free-energy functionals for trajectory ensembles to identify dynamical features reminiscent of hydrophobic behavior observed near the liquid-vapor transition in the presence of solutes in water. We show that these phenomena are observable in experiments and discuss the impact of common imperfections, such as readout errors and disordered interactions.

Introduction.— Quantum simulators have nowadays become a versatile tool to probe both equilibrium [1–4] and non-equilibrium [5–10] many-body quantum physics. For instance, they provide a handle to explore thermalization in closed quantum systems [11–13] or the lack of it in the presence of ergodicity-breaking mechanisms [14–17]. These platforms also allow us to investigate complex many-body dynamics, e.g., stemming from Hilbert space fragmentation [18–23] and from the presence of quantum scars [24–26].

Recent technical advances with quantum simulators permit fast high-fidelity mid-circuit readout [27–31]. Several works, both experimental and theoretical, have exploited this capability to explore the interplay between coherent and dissipative processes as well as to engineer non-equilibrium many-body phases of matter [32–41]. Mid-circuit measurements further offer a way to actively intervene in the system dynamics, e.g., through feedback operations conditional on the measurement outcomes [42–44]. This turns out to be crucial, e.g., for the implementation of quantum error correction strategies [45–50]. Moreover, as recently discovered for continuously-monitored open quantum systems [51–57], the statistics of mid-circuit measurements may be a resource for quantum-enhanced sensing [58] or for characterizing bath correlation functions [59, 60].

Mid-circuit measurements are a means to manipulate quantum states or to enhance the performance of quantum devices. However, monitoring the measurement results of a selected subset of degrees of freedom [cf. Fig. 1(a)] also naturally yields space-time resolved quantum trajectories. This information—which is directly accessible in experiments—can be analyzed

to probe many-body quantum dynamics without the need of state tomography and/or postselection [see, e.g., Fig. 1(c,d)]. In fact, the close resemblance of these space-time records to microscopic configurations of classical spin systems, see Fig. 1(d), motivates their analysis through thermodynamic concepts [61–64]. While this idea has been successfully applied to study classical stochastic processes [65–79], much less has been established in many-body quantum settings, in particular when going beyond effectively classical theories [80–84] and few-body cases [84–93] (see however Ref. [94] for a study on a continuous-time open quantum system).

In this paper, we explore large-scale quantum trajectories of a strongly-interacting monitored quantum system [cf. Fig. 1(a,b)] and demonstrate how these can be used to unveil and characterize emergent dynamical behavior. Using tensor-network simulations, we observe coexistence of active and inactive regions in the space-time record of ancillary measurement outcomes [see an example in Fig. 1(c,d)]. We introduce dynamical free-energy functions to characterize the statistics of inactive regions. This allows us to reveal phenomena akin to the *hydrophobic effect* and the *hydrophobic collapse* describing the behavior of solutes near the water-vapor phase transition. Our study highlights that modern quantum simulators with the capability to observe space-time resolved quantum trajectories open a new window for research into complex dynamical phenomena.

Discrete-time quantum trajectories.— The setup we focus on is motivated, for instance, by recent experiments with dual-species Rydberg atoms [31]. We consider a quantum system (S) composed of L atoms, each

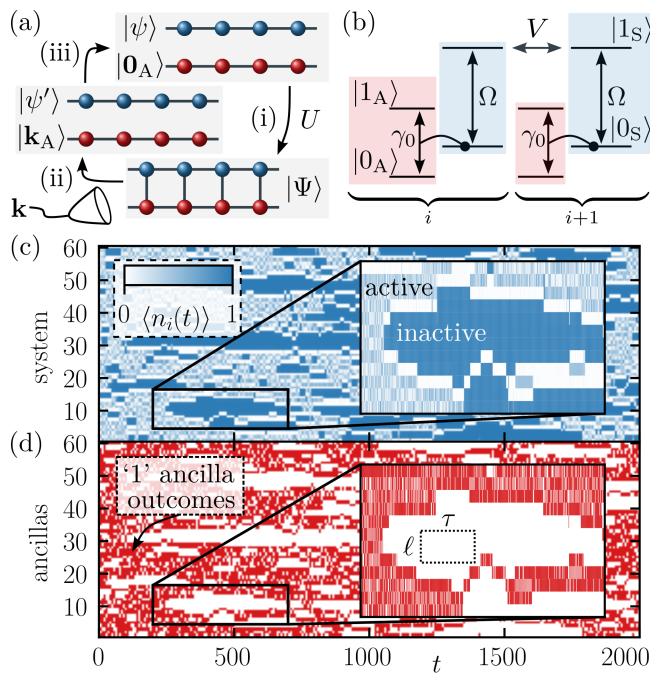


FIG. 1. **Dynamical coexistence in the space-time of monitored quantum systems.** (a) The dynamics is realized as follows: (i) the system of interest interacts with a set of ancillary degrees of freedom; (ii) the ancillas are projectively measured, providing the vector \mathbf{k} with all binary outcomes $\mathbf{k} = (k_1, \dots, k_L)$; (iii) the ancillas are reset to their reference state $|0_A\rangle$. (b) Sketch of the dynamical processes with system atoms in blue and ancillas in red [see Eq. (2) below]. (c,d) Stochastic dynamical realization of the quantum expectation of the local density of excited states ($|1_S\rangle$), $\langle n_i(t) \rangle$, and corresponding measurement history, for $L = 60$, $\Omega\Delta t = 1.25$, $\gamma = 3\Omega$ and $V = 5.875\Omega$. We observe distinct dynamical phases: an active one with rapidly varying local density and a large number of ‘1’ measurement outcomes for the ancilla, and an inactive one with atoms approximately frozen in the excited state and extended space-time regions characterized by ‘0’ measurement outcomes. In one such region, we highlight a $\ell \times \tau$ cluster solely composed by ‘0’ outcomes. Note that only panel (d) can be obtained from a single experimental run.

one coupled to an ancilla (A), i.e., an auxiliary degree of freedom, see Fig. 1(a) and Refs. [93, 95–97]. The latter are subject to mid-circuit measurement, which allows for indirect readout of system properties. Both atoms and ancillas consist of two-level systems with (computational) basis states $\{|0_{S/A}\rangle, |1_{S/A}\rangle\}$. The dynamics effectively occurs in discrete-time and a single update is obtained as follows. The system, described by the state $|\psi\rangle$, and the ancillas, initialized in state $|0_A\rangle = |0_A\rangle^{\otimes L}$, unitarily interact as described by the operator U . After the interaction, their state reads

$$|\Psi\rangle = U(|\psi\rangle \otimes |0_A\rangle) = \sum_{\{\mathbf{k}\}} K_{\mathbf{k}} |\psi\rangle \otimes |\mathbf{k}_A\rangle, \quad (1)$$

where $\mathbf{k} = (k_1, \dots, k_L)$, with $k_i \in \{0, 1\}$, and $K_{\mathbf{k}} =$

$\langle \mathbf{k}_A | U | 0_A \rangle$ are Kraus operators solely acting on the system [98]. The ancillary degrees of freedom are then projectively measured in the computational basis, which selects a single term in the superposition appearing on the right hand side of Eq. (1). Finally, ancillas are reset to their reference state in preparation for the next update. Each measurement outcome \mathbf{k} has probability $\pi(\mathbf{k}) = \|K_{\mathbf{k}} |\psi\rangle\|^2$ and is associated with the conditional system state $|\psi'\rangle = K_{\mathbf{k}} |\psi\rangle / \|K_{\mathbf{k}} |\psi\rangle\|$. Iterating this procedure T times gives rise to a stochastic realization $|\psi_0\rangle = |0_S\rangle \rightarrow \dots \rightarrow |\psi_T\rangle$ and the corresponding quantum trajectory $\eta(T) = [\mathbf{k}(t)]_{t=1}^T$, encoding the space-time record of ancillary measurement outcomes.

Concretely, we consider the unitary $U = e^{-iH_{\text{CM}}\Delta t}$, where Δt is the interaction time, and

$$H_{\text{CM}} = \left(\Omega \sum_{i=1}^L \sigma_i^x + V \sum_{i=1}^{L-1} n_i n_{i+1} \right) \otimes \mathbb{1} + \gamma_0 \sum_{i=1}^L P_i \otimes \sigma_i^x, \quad (2)$$

with $\sigma^x = |0\rangle\langle 1| + \text{h.c.}$, $n = |1\rangle\langle 1|$, and $P = |0\rangle\langle 0|$ [93]. The left hand side of the tensor product is for system operators while the right hand side for ancillas [see Fig. 1(b)]. The first term in Eq. (2) describes a chain of resonantly-driven Rydberg atoms (Rabi frequency Ω) with nearest-neighbor interaction strength V . The second term in Eq. (2) enforces a driving on the ancillas with frequency $\gamma_0 = \sqrt{\gamma/\Delta t}$ conditional on the corresponding system atom being in $|0_S\rangle$, which allows one to probe the ground-state population [99]. In the following, we explore the dynamics of such a system by developing ad-hoc tensor-network techniques to access large system sizes, see the Supplemental Material [100] for details.

Quantum states vs. quantum trajectories.—

We are interested in characterizing dynamical features of the model introduced above. This can be achieved, for instance, by analyzing the quantum state $|\psi_t\rangle$ in single realizations of the dynamics, e.g., by considering the expectation value $\langle n_i(t) \rangle = \langle \psi_t | n_i | \psi_t \rangle$ of the local Rydberg density [see an example in Fig. 1(c)]. For sufficiently strong interactions ($V \gg \Omega$) [93], this shows clear signatures of coexistence in terms of regions with rapid oscillations in $\langle n_i(t) \rangle$ and others where atoms remain stuck in the Rydberg state. However, for a single realization, this quantity—albeit theoretically accessible—cannot be measured in practice. The reason is that to estimate expectation values from experimental data one needs to collect measurements of the Rydberg density from the same stochastic realizations of the dynamics. This is not possible since the probability of observing the same trajectory twice is essentially zero. In the context of entanglement phase transitions, this is referred to as the postselection problem [117–120]. Experimentally accessible expectation values are those associated with the average state ρ evolving through the Kraus

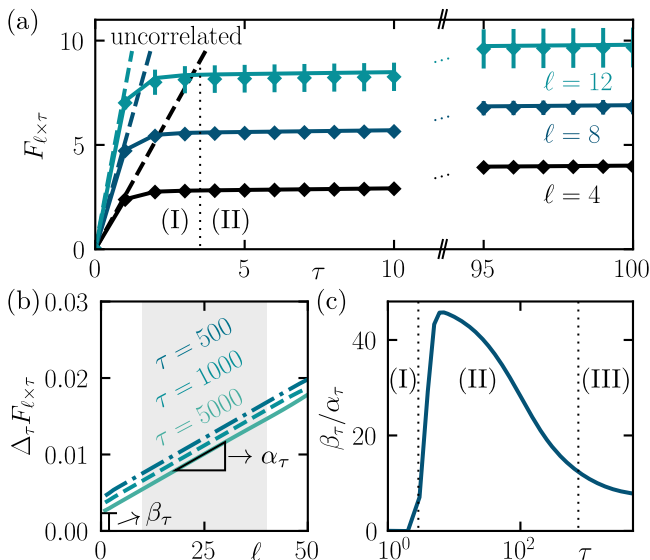


FIG. 2. **Statistics of inactive space-time cluster.** (a) Dynamical free energy (negative log of the probability) of finding an inactive cluster with fixed spatial size ℓ as a function of the temporal extension τ . We show the empirically extracted probability from 20 quantum trajectories of 100 000 time steps each (symbols with errorbars representing the statistical uncertainty) and the theoretical prediction for the ensemble average (solid lines). The dashed lines provide the dynamical free energy in the case of uncorrelated outcomes for comparison. (b,c) Scaling behavior of the free-energy increment $\Delta_\tau F_{\ell \times \tau}$ [cf. Eq. (4)]. For every fixed temporal extension τ , we infer α_τ and β_τ from the gray shaded region.

map $\mathcal{E}[\rho] = \sum_{\{\mathbf{k}\}} K_{\mathbf{k}\rho} K_{\mathbf{k}}^\dagger$ [97]. However, the information about the coexistence observed in Fig. 1(c) is washed out in this average state, which eventually converges to a structureless, infinite-temperature state in the long-time limit [93].

This shows the advantage of focusing an analysis of the dynamics on space-time resolved quantum trajectories, like the one shown in Fig. 1(d). In contrast to quantum expectation values of the stochastic state, quantum trajectories are directly accessible in single experimental runs and characterizing their behavior does not require any postselection. Moreover, as demonstrated by the appearance of large inactive clusters—domains of ‘0’ measurement outcomes—immersed in otherwise active regions (with a high rate of measurement outcomes ‘1’), these contain similar information about the system’s dynamical behavior as that displayed by the Rydberg density [cf. Fig. 1(c,d)]. Motivated by this and borrowing ideas from works on classical models [111–113], we now analyze the statistics of large-scale inactive clusters in terms of thermodynamic concepts.

Statistics of inactive space-time clusters.— The extension of inactive dynamical regions is characterized through the stationary probability $p_{\ell \times \tau}$ of finding an in-

active cluster of space-time size $\ell \times \tau$ in the quantum trajectory, see an example in Fig. 1(d). It is instructive to describe such a probability by means of an effective “dynamical free energy”, given by

$$F_{\ell \times \tau} = -\log p_{\ell \times \tau}. \quad (3)$$

This quantity indeed allows us to understand how the probability decays in terms of an “energetic” and “entropic” cost of accommodating inactive clusters in quantum trajectories. As shown in Fig. 2(a), $F_{\ell \times \tau}$ exhibits distinct behavior as a function of τ for fixed ℓ : (I) a regime effectively scaling with the area of the cluster, characterized by a steep growth for $\tau \lesssim 3$, which strongly depends on ℓ , followed by (II) a regime effectively scaling with the perimeter of the cluster, with a much slower growth for $\tau \gtrsim 3$, only weakly depending on ℓ . The dynamical free energy thus markedly differs from that of completely uncorrelated trajectories, namely $\ell \tau F_{1 \times 1}$ [see dashed lines in Fig. 2(a)].

The crossover from an area to a perimeter scaling can signal the proximity to a first-order dynamical phase transition [111–113]. The underlying idea builds on the behavior of solutes near the liquid-vapor transition [121–123]. Here, the free energy for encapsulating a small solute inside a vapor bubble shows a cost that scales with the size of bubble itself. For larger solutes, instead, the free energy solely scales as the interface between water and vapor.

Assuming the dynamical free energy $F_{\ell \times \tau}$ to solely consist of an area and a perimeter contribution (see the Supplemental Material [100] for details), its increment, $\Delta_\tau F_{\ell \times \tau}$, upon extending the cluster size by one unit of time at fixed ℓ takes the form

$$\Delta_\tau F_{\ell \times \tau} = F_{\ell \times (\tau+1)} - F_{\ell \times \tau} = \alpha_\tau \ell + \beta_\tau. \quad (4)$$

Such a quantity is essentially related to a temporal “interface tension” of the inactive cluster. The plot in Fig. 2(b) confirms the linear behavior of Eq. (4), which allows us to determine the area and perimeter contributions in terms of their respective coefficients α_τ and β_τ . For any $\alpha_\tau > 0$, the area contribution would eventually dominate in the limit of very large inactive clusters ($\ell \rightarrow \infty$). On the other hand, for intermediate cluster sizes, the dominant scaling behavior of the dynamical free energy can be understood by comparing the cluster’s spatial extension, i.e., $\ell \approx 10$, to the fraction β_τ / α_τ [cf. Eq. (4)]. In Fig. 2(c), we highlight two area-dominated regimes, $\beta_\tau < \alpha_\tau \ell$, appearing for small and very large τ , and a perimeter-dominated one, $\beta_\tau > \alpha_\tau \ell$, emerging at intermediate values of τ . The first area-to-perimeter crossover is reminiscent of the hydrophobic effect close to the water-to-vapor transition. A key difference, also with respect to results for the classical models [111–113], lies in the re-entrant area-dominated scaling for large τ . The latter is essentially due to the fact that, while transitions to or from

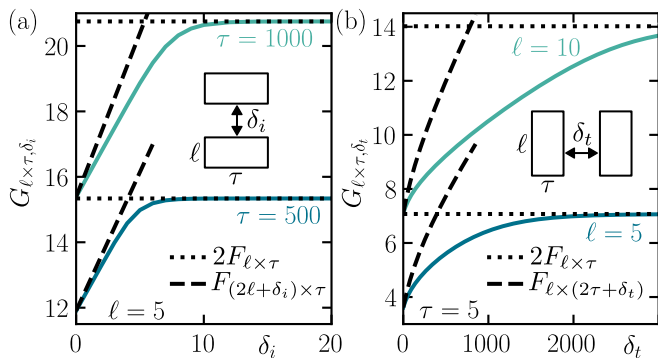


FIG. 3. **Attraction between inactive clusters.** Dynamical free energy for two $\ell \times \tau$ inactive clusters separated by either (a) δ_i in space or (b) δ_t in time. In both panels, the dotted line represents the dynamical free energy for independent clusters, while the dashed line represents that for an inactive cluster of size $(2\ell + \delta_i) \times \tau$ [panel (a)] or $\ell \times (2\tau + \delta_t)$ [panel (b)], enclosing the two considered inactive clusters.

the Rydberg state are off-resonant in the presence of excited neighbors and strong interactions, they can still occur even in the middle of an otherwise inactive region. This hence allows for ‘1’ measurement outcomes that break up the inactive cluster and provides an underlying area contribution to the dynamical free energy, which dominates at very large cluster sizes.

Attraction between inactive clusters.— Extending the discussion of inactive regions, we now investigate the dynamical free energy $G_{\ell \times \tau, \delta_i}$ ($G_{\ell \times \tau, \delta_t}$) associated with the probability of observing two identical inactive clusters of size $\ell \times \tau$ separated by a spatial (temporal) distance δ_i (δ_t). This quantity is shown in Fig. 3 and also exhibits crossover behavior. For large distances between clusters, the dynamical free energy of the two clusters saturates to a constant value, essentially given by the free energy of two independent clusters, namely $2F_{\ell \times \tau}$ (black dotted lines). For shorter distances, instead, the dynamical free energy is initially dominated by the free energy of a single larger cluster enclosing the two, i.e., $G_{\ell \times \tau, \delta_i} \approx F_{(2\ell + \delta_i) \times \tau}$ and $G_{\ell \times \tau, \delta_t} \approx F_{\ell \times (2\tau + \delta_t)}$ for spatial and temporal separation, respectively (black dashed lines). As the dynamical free energy provides a “cost” for sustaining the configuration, its decrease for decreasing distances entails an effective attractive force between clusters, suggesting that it is likely to find clusters to merge together. This behavior is reminiscent of the so-called “hydrophobic collapse”.

As it can be appreciated by comparing Fig. 3(a) and Fig. 3(b), a marked difference emerges between the case of spatially or temporally separated inactive clusters. As the spatial separation increases, the dynamical free energy rapidly approaches the limit of uncorrelated inactive clusters. In contrast, temporal correlations between inactive clusters persist over significantly longer

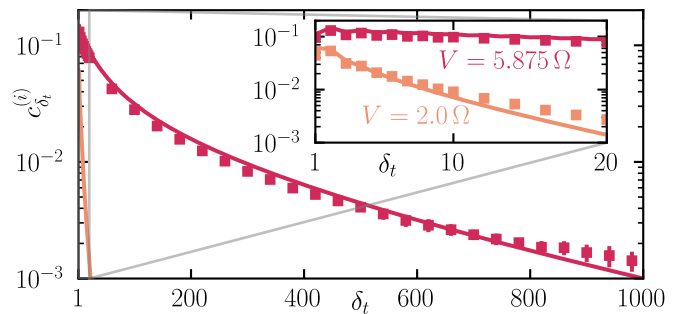


FIG. 4. **Autocorrelation function.** The solid line provides the behavior of the ensemble-average autocorrelation function, for the ideal case, as a function of the time difference δ_t [cf. Eq. (5)]. The symbols are results obtained from quantum trajectories considering the disordered couplings (see text) as well as a probability $p_{\text{err}} = 2\%$ for measurement readout errors. The top curve is for $V = 5.875 \Omega$ (red), where trajectories display dynamical phase coexistence. The bottom curve is for $V = 2 \Omega$ (orange), which does not display such coexistence behavior. The inset shows a magnification of the initial transient behavior.

time-scales due to the difference in temporal and spatial interface tensions (see the Supplemental Material [100]).

Role of experimental imperfections.— In order to explore the robustness of the observed phenomenology to experimental imperfections, we consider, as exemplary case, the autocorrelation function

$$c_{\delta_t}^{(i)}(t) = \overline{k_i(t)k_i(t - \delta_t)} - \overline{k_i(t)} \overline{k_i(t - \delta_t)}, \quad (5)$$

with $\overline{f(t)}$ denoting the ensemble average of a dynamical quantity $f(t)$ over all quantum trajectories [93]. We focus on its behavior at stationarity. Furthermore, since we expect measurements to be only marginally influenced by the position along the chain, we also average over all ancilla sites i far enough from the boundaries. Common experimental imperfections are related to disorder in the interaction strengths between atoms and ancillas, as well as between atoms themselves. To account for this, we consider locally varying coupling constants V and γ , which are uniformly distributed in a range of $\pm\Omega$. Additionally, we also include measurement readout errors, characterized by a probability p_{err} of flipping the ancilla outcome.

The autocorrelation function given by Eq. (4) is displayed in Fig. 4. It shows slow relaxation towards uncorrelated measurements. This slowness is in fact a result of the correlated trajectory dynamics, i.e. the coexistence of active and inactive space-time regions. The figure also compares the autocorrelation obtained through an ideal ensemble average with the one obtained by gathering statistics from quantum trajectories of more realistic dynamics. This highlights that such a quantity is robust to experimental imperfections

[100]. For comparison we also show the autocorrelation function at $V = 2\Omega$. Here the system relaxes uniformly and correlations decay orders of magnitude faster.

Outlook.— Mid-circuit measurements in quantum simulation provide access to space-time resolved information on many-body quantum dynamics. Already the model analyzed in this paper shows interesting emergent dynamical behavior. Experiments with quantum simulators will allow for the study of more complex cases beyond the reach of tensor network computations. These include higher-dimensional systems and many-body dynamics, which generate more entanglement than the Rydberg density-density interaction considered here. This may lead to new collective features in trajectory thermodynamics or even to the emergence of new universality classes.

The code and data that support the findings of this work are available on Zenodo [124].

Acknowledgements. — We thank Hannes Bernien, Peter Sollich, Juan P. Garrahan and Adam Gammon-Smith for fruitful discussions. Tensor network calculations were performed using the `ITensors.jl` library [102]. We acknowledge funding from the Deutsche Forschungsgemeinschaft (DFG, German Research Foundation) under Germany’s Excellence Strategy – EXC-2111 – 390814868, through the Research Unit FOR 5413/1, Grant No. 465199066, through the Research Unit FOR 5522/1, Grant No. 499180199, and through the state of Baden-Württemberg through bwHPC and the German Research Foundation (DFG) through grant no INST 40/575-1 FUGG (JUSTUS 2 cluster). This project has also received funding from the European Union’s Horizon Europe research and innovation program under Grant Agreement No. 101046968 (BRISQ). C.D.F. acknowledges support from the Alexander von Humboldt Foundation through a post-doctoral research fellowship. This work is supported by ERC grant OPEN-2QS (Grant No. 101164443, <https://doi.org/10.3030/101164443>).

[1] H.-J. Shao, Y.-X. Wang, D.-Z. Zhu, Y.-S. Zhu, H.-N. Sun, S.-Y. Chen, C. Zhang, Z.-J. Fan, Y. Deng, X.-C. Yao, *et al.*, Antiferromagnetic phase transition in a 3D fermionic Hubbard model, *Nature* **632**, 267 (2024).
 [2] A. Impertro, S. Huh, S. Karch, J. F. Wienand, I. Bloch, and M. Aidelsburger, Strongly interacting Meissner phases in large bosonic flux ladders, *Nat. Phys.* **21**, 895 (2025).
 [3] A. Schuckert, O. Katz, L. Feng, E. Crane, A. De, M. Hafezi, A. V. Gorshkov, and C. Monroe, Observation of a finite-energy phase transition in a one-dimensional

quantum simulator, *Nat. Phys.* **21**, 374 (2025).
 [4] R. Haghshenas, E. Chertkov, M. DeCross, T. M. Gatterman, J. A. Gerber, K. Gilmore, D. Gresh, N. Hewitt, C. V. Horst, M. Matheny, *et al.*, Probing Critical States of Matter on a Digital Quantum Computer, *Phys. Rev. Lett.* **133**, 266502 (2024).
 [5] C. Gross and I. Bloch, Quantum simulations with ultracold atoms in optical lattices, *Science* **357**, 995 (2017).
 [6] B. Fauseweh, Quantum many-body simulations on digital quantum computers: State-of-the-art and future challenges, *Nat. Commun.* **15**, 2123 (2024).
 [7] N. Darkwah Oppong, G. Pasqualetti, O. Bettermann, P. Zechmann, M. Knap, I. Bloch, and S. Fölling, Probing Transport and Slow Relaxation in the Mass-Imbalanced Fermi-Hubbard Model, *Phys. Rev. X* **12**, 031026 (2022).
 [8] Y. Kim, A. Eddins, S. Anand, K. X. Wei, E. van den Berg, S. Rosenblatt, H. Nayfeh, Y. Wu, M. Zaletel, K. Temme, and A. Kandala, Evidence for the utility of quantum computing before fault tolerance, *Nature* **618**, 500 (2023).
 [9] S.-A. Guo, Y.-K. Wu, J. Ye, L. Zhang, W.-Q. Lian, R. Yao, Y. Wang, R.-Y. Yan, Y.-J. Yi, Y.-L. Xu, *et al.*, A site-resolved two-dimensional quantum simulator with hundreds of trapped ions, *Nature* **630**, 613 (2024).
 [10] D. A. Abanin, R. Acharya, L. Aghababaie-Beni, G. Aigeldinger, A. Ajoy, R. Alcaraz, I. Aleiner, T. I. Andersen, M. Ansmann, F. Arute, *et al.*, Constructive interference at the edge of quantum ergodic dynamics, [arXiv:2506.10191](https://arxiv.org/abs/2506.10191) (2025).
 [11] A. M. Kaufman, M. E. Tai, A. Lukin, M. Rispoli, R. Schittko, P. M. Preiss, and M. Greiner, Quantum thermalization through entanglement in an isolated many-body system, *Science* **353**, 794 (2016).
 [12] Z.-Y. Zhou, G.-X. Su, J. C. Halimeh, R. Ott, H. Sun, P. Hauke, B. Yang, Z.-S. Yuan, J. Berges, and J.-W. Pan, Thermalization dynamics of a gauge theory on a quantum simulator, *Science* **377**, 311 (2022).
 [13] T. I. Andersen, N. Astrakhantsev, A. H. Karamlou, J. Berndtsson, J. Motruk, A. Szasz, J. A. Gross, A. Schuckert, T. Westerhout, Y. Zhang, *et al.*, Thermalization and criticality on an analogue–digital quantum simulator, *Nature* **638**, 79 (2025).
 [14] M. Schreiber, S. S. Hodgman, P. Bordia, H. P. Lüschen, M. H. Fischer, R. Vosk, E. Altman, U. Schneider, and I. Bloch, Observation of many-body localization of interacting fermions in a quasirandom optical lattice, *Science* **349**, 842 (2015).
 [15] J.-y. Choi, S. Hild, J. Zeiher, P. Schauß, A. Rubio-Abadal, T. Yefsah, V. Khemani, D. A. Huse, I. Bloch, and C. Gross, Exploring the many-body localization transition in two dimensions, *Science* **352**, 1547 (2016).
 [16] W. Morong, S. R. Muleady, I. Kimchi, W. Xu, R. M. Nandkishore, A. M. Rey, and B. DeMarco, Disorder-controlled relaxation in a three-dimensional Hubbard model quantum simulator, *Phys. Rev. Research* **3**, L012009 (2021).
 [17] Q. Guo, C. Cheng, Z.-H. Sun, Z. Song, H. Li, Z. Wang, W. Ren, H. Dong, D. Zheng, Y.-R. Zhang, *et al.*, Observation of energy-resolved many-body localization, *Nat. Phys.* **17**, 234 (2021).
 [18] S. Scherg, T. Kohlert, P. Sala, F. Pollmann, B. Hebbe Madhusudhana, I. Bloch, and M. Aidels-

- burger, Observing non-ergodicity due to kinetic constraints in tilted Fermi-Hubbard chains, *Nat. Commun.* **12**, 4490 (2021).
- [19] D. Adler, D. Wei, M. Will, K. Srakaew, S. Agrawal, P. Weckesser, R. Moessner, F. Pollmann, I. Bloch, and J. Zeiher, Observation of Hilbert space fragmentation and fractonic excitations in 2D, *Nature* **636**, 80 (2024).
- [20] Y.-H. Shi, Z.-H. Sun, Y.-Y. Wang, Z.-A. Wang, Y.-R. Zhang, W.-G. Ma, H.-T. Liu, K. Zhao, J.-C. Song, G.-H. Liang, *et al.*, Probing spin hydrodynamics on a superconducting quantum simulator, *Nat. Commun.* **15**, 7573 (2024).
- [21] S. Karch, S. Bandyopadhyay, Z.-H. Sun, A. Impertro, S. Huh, I. P. Rodríguez, J. F. Wienand, W. Ketterle, M. Heyl, A. Polkovnikov, *et al.*, Probing quantum many-body dynamics using subsystem Loschmidt echos, [arXiv:2501.16995](https://arxiv.org/abs/2501.16995) (2025).
- [22] L. Zhao, P. R. Datla, W. Tian, M. M. Aliyu, and H. Loh, Observation of Quantum Thermalization Restricted to Hilbert Space Fragments and \mathbb{Z}_{2k} Scars, *Phys. Rev. X* **15**, 011035 (2025).
- [23] K. Honda, Y. Takasu, S. Goto, H. Kazuta, M. Kunimi, I. Danshita, and Y. Takahashi, Observation of slow relaxation due to hilbert space fragmentation in strongly interacting bose-hubbard chains, *Sci. Adv.* **11**, eadv3255 (2025).
- [24] H. Bernien, S. Schwartz, A. Keesling, H. Levine, A. Omran, H. Pichler, S. Choi, A. S. Zibrov, M. Endres, M. Greiner, *et al.*, Probing many-body dynamics on a 51-atom quantum simulator, *Nature* **551**, 579 (2017).
- [25] G.-X. Su, H. Sun, A. Hudomal, J.-Y. Desaulles, Z.-Y. Zhou, B. Yang, J. C. Halimeh, Z.-S. Yuan, Z. Papić, and J.-W. Pan, Observation of many-body scarring in a Bose-Hubbard quantum simulator, *Phys. Rev. Research* **5**, 023010 (2023).
- [26] Z. Bao, S. Xu, Z. Song, K. Wang, L. Xiang, Z. Zhu, J. Chen, F. Jin, X. Zhu, Y. Gao, *et al.*, Creating and controlling global Greenberger-Horne-Zeilinger entanglement on quantum processors, *Nat. Commun.* **15**, 8823 (2024).
- [27] A. D. Córcoles, M. Takita, K. Inoue, S. Lekuch, Z. K. Mineev, J. M. Chow, and J. M. Gambetta, Exploiting Dynamic Quantum Circuits in a Quantum Algorithm with Superconducting Qubits, *Phys. Rev. Lett.* **127**, 100501 (2021).
- [28] J. M. Pino, J. M. Dreiling, C. Figgatt, J. P. Gaebler, S. A. Moses, M. S. Allman, C. H. Baldwin, M. Foss-Feig, D. Hayes, K. Mayer, *et al.*, Demonstration of the trapped-ion quantum CCD computer architecture, *Nature* **592**, 209 (2021).
- [29] E. Deist, Y.-H. Lu, J. Ho, M. K. Pasha, J. Zeiher, Z. Yan, and D. M. Stamper-Kurn, Mid-Circuit Cavity Measurement in a Neutral Atom Array, *Phys. Rev. Lett.* **129**, 203602 (2022).
- [30] T. M. Graham, L. Phuttitarn, R. Chinnarasu, Y. Song, C. Poole, K. Jooya, J. Scott, A. Scott, P. Eichler, and M. Saffman, Midcircuit Measurements on a Single-Species Neutral Alkali Atom Quantum Processor, *Phys. Rev. X* **13**, 041051 (2023).
- [31] S. Anand, C. E. Bradley, R. White, V. Ramesh, K. Singh, and H. Bernien, A dual-species Rydberg array, *Nat. Phys.* **20**, 1744 (2024).
- [32] P. M. Harrington, E. J. Mueller, and K. W. Murch, Engineered dissipation for quantum information science, *Nat. Rev. Phys.* **4**, 660 (2022).
- [33] S. Diehl, A. Micheli, A. Kantian, B. Kraus, H. P. Büchler, and P. Zoller, Quantum states and phases in driven open quantum systems with cold atoms, *Nat. Phys.* **4**, 878 (2008).
- [34] F. Verstraete, M. M. Wolf, and J. Ignacio Cirac, Quantum computation and quantum-state engineering driven by dissipation, *Nat. Phys.* **5**, 633 (2009).
- [35] Z.-P. Cian, G. Zhu, S.-K. Chu, A. Seif, W. DeGottardi, L. Jiang, and M. Hafezi, Photon Pair Condensation by Engineered Dissipation, *Phys. Rev. Lett.* **123**, 063602 (2019).
- [36] A. Paviglianiti and A. Silva, Enhancing revivals via projective measurements in a quantum scarred system, [arXiv:2503.2261](https://arxiv.org/abs/2503.2261) (2025).
- [37] E. Chertkov, Z. Cheng, A. C. Potter, S. Gopalakrishnan, T. M. Gatterman, J. A. Gerber, K. Gilmore, D. Gresh, A. Hall, A. Hankin, *et al.*, Characterizing a non-equilibrium phase transition on a quantum computer, *Nat. Phys.* **19**, 1 (2023).
- [38] X. Mi, A. A. Michailidis, S. Shabani, K. C. Miao, P. V. Klimov, J. Lloyd, E. Rosenberg, R. Acharya, I. Aleiner, T. I. Andersen, *et al.*, Stable quantum-correlated many-body states through engineered dissipation, *Science* **383**, 1332 (2024).
- [39] K. Sun, M. Kang, H. Nuomin, G. Schwartz, D. N. Beratan, K. R. Brown, and J. Kim, Quantum simulation of spin-boson models with structured bath, *Nat. Commun.* **16**, 4042 (2025).
- [40] L. Li, T. Liu, X.-Y. Guo, H. Zhang, S. Zhao, Z.-A. Wang, Z. Xiang, X. Song, Y.-X. Zhang, K. Xu, *et al.*, Observation of multiple steady states with engineered dissipation, *npj Quantum Inf.* **11**, 1 (2025).
- [41] C. Chen, K. Tang, Y. Zhou, K. Yi, X. Zhang, X. Zhang, H. Guo, S. Liu, Y. Chen, T. Yan, and D. Yu, Hardware-efficient stabilization of entanglement via engineered dissipation in superconducting circuits, *Phys. Rev. Research* **7**, L022018 (2025).
- [42] L. Steffen, Y. Salathe, M. Oppliger, P. Kurpiers, M. Baur, C. Lang, C. Eichler, G. Puebla-Hellmann, A. Fedorov, and A. Wallraff, Deterministic quantum teleportation with feed-forward in a solid state system, *Nature* **500**, 319 (2013).
- [43] Z. K. Mineev, S. O. Mundhada, S. Shankar, P. Reinhold, R. Gutiérrez-Jáuregui, R. J. Schoelkopf, M. Mirrahimi, H. J. Carmichael, and M. H. Devoret, To catch and reverse a quantum jump mid-flight, *Nature* **570**, 200 (2019).
- [44] M. Iqbal, N. Tantivasadakarn, T. M. Gatterman, J. A. Gerber, K. Gilmore, D. Gresh, A. Hankin, N. Hewitt, C. V. Horst, M. Matheny, *et al.*, Topological order from measurements and feed-forward on a trapped ion quantum computer, *Commun. Phys.* **7**, 1 (2024).
- [45] J. Cramer, N. Kalb, M. A. Rol, B. Hensen, M. S. Blok, M. Markham, D. J. Twitchen, R. Hanson, and T. H. Taminiau, Repeated quantum error correction on a continuously encoded qubit by real-time feedback, *Nat. Commun.* **7**, 11526 (2016).
- [46] S. Krinner, N. Lacroix, A. Remm, A. Di Paolo, E. Genois, C. Leroux, C. Hellings, S. Lazar, F. Swiadek, J. Herrmann, *et al.*, Realizing repeated quantum error correction in a distance-three surface code, *Nature* **605**, 669 (2022).
- [47] K. Singh, C. E. Bradley, S. Anand, V. Ramesh,

- R. White, and H. Bernien, Mid-circuit correction of correlated phase errors using an array of spectator qubits, *Science* **380**, 1265 (2023).
- [48] L. Postler, F. Butt, I. Pogorelov, C. D. Marciniak, S. Heußen, R. Blatt, P. Schindler, M. Rispler, M. Müller, and T. Monz, Demonstration of Fault-Tolerant Steane Quantum Error Correction, *PRX Quantum* **5**, 030326 (2024).
- [49] D. Bluvstein, S. J. Evered, A. A. Geim, S. H. Li, H. Zhou, T. Manovitz, S. Ebadi, M. Cain, M. Kalinowski, D. Hangleiter, *et al.*, Logical quantum processor based on reconfigurable atom arrays, *Nature* **626**, 58 (2024).
- [50] R. Acharya, D. A. Abanin, L. Aghababaie-Beni, I. Aleiner, T. I. Andersen, M. Ansmann, F. Arute, K. Arya, A. Asfaw, N. Astrakhantsev, *et al.*, Quantum error correction below the surface code threshold, *Nature* **638**, 920 (2024).
- [51] K. Macieszczak, M. Guță, I. Lesanovsky, and J. P. Garrahan, Dynamical phase transitions as a resource for quantum enhanced metrology, *Phys. Rev. A* **93**, 022103 (2016).
- [52] T. Ilias, D. Yang, S. F. Huelga, and M. B. Plenio, Criticality-Enhanced Quantum Sensing via Continuous Measurement, *PRX Quantum* **3**, 010354 (2022).
- [53] A. Cabot, F. Carollo, and I. Lesanovsky, Exploiting nonequilibrium phase transitions and strong symmetries for continuous measurement of collective observables, *Phys. Rev. A* **110**, L060601 (2024).
- [54] R. Mattes, A. Cabot, F. Carollo, and I. Lesanovsky, Designing open quantum systems for enabling quantum enhanced sensing through classical measurements, [arXiv:2505.08756](https://arxiv.org/abs/2505.08756) (2025).
- [55] S. Midha and S. Gopalakrishnan, Metrology of open quantum systems from emitted radiation, [arXiv:2504.13815](https://arxiv.org/abs/2504.13815) (2025).
- [56] A. Khan, F. Albarelli, and A. Datta, A tensor network approach to sensing quantum light-matter interactions, [arXiv:2504.12399](https://arxiv.org/abs/2504.12399) (2025).
- [57] G. Lee, R. Belyansky, L. Jiang, and A. A. Clerk, Timescales, squeezing and heisenberg scalings in many-body continuous sensing, [arXiv:2505.04591](https://arxiv.org/abs/2505.04591) (2025).
- [58] T. Ilias, Biasing quantum trajectories for enhanced sensing, *Phys. Rev. A* **111**, 042432 (2025).
- [59] P. Wang, C. Chen, X. Peng, J. Wrachtrup, and R.-B. Liu, Characterization of Arbitrary-Order Correlations in Quantum Baths by Weak Measurement, *Phys. Rev. Lett.* **123**, 050603 (2019).
- [60] Z. Wu, P. Wang, T. Wang, Y. Li, R. Liu, Y. Chen, X. Peng, and R.-B. Liu, Selective Detection of Dynamics-Complete Set of Correlations via Quantum Channels, *Phys. Rev. Lett.* **132**, 200802 (2024).
- [61] H. Touchette, The large deviation approach to statistical mechanics, *Phys. Rep.* **478**, 1 (2009).
- [62] J. P. Garrahan and I. Lesanovsky, Thermodynamics of Quantum Jump Trajectories, *Phys. Rev. Lett.* **104**, 160601 (2010).
- [63] R. Chetrite and H. Touchette, Nonequilibrium Microcanonical and Canonical Ensembles and Their Equivalence, *Phys. Rev. Lett.* **111**, 120601 (2013).
- [64] M. Cech, I. Lesanovsky, and F. Carollo, Thermodynamics of Quantum Trajectories on a Quantum Computer, *Phys. Rev. Lett.* **131**, 120401 (2023).
- [65] R. L. Jack and P. Sollich, Large Deviations and Ensembles of Trajectories in Stochastic Models, *Prog. Theor. Phys. Suppl.* **184**, 304 (2010).
- [66] D. Chandler and J. P. Garrahan, Dynamics on the Way to Forming Glass: Bubbles in Space-Time, *Annu. Rev. Phys. Chem.* **61**, 191 (2010).
- [67] T. Bodineau, V. Lecomte, and C. Toninelli, Finite Size Scaling of the Dynamical Free-Energy in a Kinetically Constrained Model, *J. Stat. Phys.* **147**, 1 (2012).
- [68] R. L. Jack and P. Sollich, Large deviations of the dynamical activity in the East model: analysing structure in biased trajectories, *J. Phys. A: Math. Theor.* **47**, 015003 (2013).
- [69] R. L. Jack and P. Sollich, Effective interactions and large deviations in stochastic processes, *Eur. Phys. J.: Spec. Top.* **224**, 2351 (2015).
- [70] R. Gutiérrez and J. P. Garrahan, Front propagation versus bulk relaxation in the annealing dynamics of a kinetically constrained model of ultrastable glasses, *J. Stat. Mech: Theory Exp.* **2016**, 074005 (2016).
- [71] J. P. Garrahan, Aspects of non-equilibrium in classical and quantum systems: Slow relaxation and glasses, dynamical large deviations, quantum non-ergodicity, and open quantum dynamics, *Physica A* **504**, 130 (2018).
- [72] B. Buča, J. P. Garrahan, T. Prosen, and M. Vanicat, Exact large deviation statistics and trajectory phase transition of a deterministic boundary driven cellular automaton, *Phys. Rev. E* **100**, 020103 (2019).
- [73] M. C. Bañuls and J. P. Garrahan, Using Matrix Product States to Study the Dynamical Large Deviations of Kinetically Constrained Models, *Phys. Rev. Lett.* **123**, 200601 (2019).
- [74] L. Causser, I. Lesanovsky, M. C. Bañuls, and J. P. Garrahan, Dynamics and large deviation transitions of the XOR-Fredrickson-Andersen kinetically constrained model, *Phys. Rev. E* **102**, 052132 (2020).
- [75] L. Causser, M. C. Bañuls, and J. P. Garrahan, Optimal sampling of dynamical large deviations via matrix product states, *Phys. Rev. E* **103**, 062144 (2021).
- [76] C. Casert, T. Vieijra, S. Whitelam, and I. Tamblyn, Dynamical large deviations of two-dimensional kinetically constrained models using a neural-network state ansatz, *Phys. Rev. Lett.* **127**, 120602 (2021).
- [77] L. Causser, M. C. Bañuls, and J. P. Garrahan, Finite Time Large Deviations via Matrix Product States, *Phys. Rev. Lett.* **128**, 090605 (2022).
- [78] L. Causser, J. P. Garrahan, and A. Lamacraft, Slow dynamics and large deviations in classical stochastic Fredkin chains, *Phys. Rev. E* **106**, 014128 (2022-07).
- [79] K. Sfairopoulos, L. Causser, and J. P. Garrahan, Multicriticality in stochastic dynamics protected by self-duality, [arXiv:2504.01258](https://arxiv.org/abs/2504.01258) (2025).
- [80] I. Lesanovsky and J. P. Garrahan, Kinetic Constraints, Hierarchical Relaxation, and Onset of Glassiness in Strongly Interacting and Dissipative Rydberg Gases, *Phys. Rev. Lett.* **111**, 215305 (2013).
- [81] M. M. Valado, C. Simonelli, M. D. Hoogerland, I. Lesanovsky, J. P. Garrahan, E. Arimondo, D. Ciampini, and O. Morsch, Experimental observation of controllable kinetic constraints in a cold atomic gas, *Phys. Rev. A* **93**, 040701 (2016).
- [82] E. Levi, R. Gutiérrez, and I. Lesanovsky, Quantum non-equilibrium dynamics of Rydberg gases in the presence of dephasing noise of different strengths, *J. Phys. B: At. Mol. Opt. Phys.* **49**, 184003 (2016).

- [83] C. Pérez-Espigares, I. Lesanovsky, J. P. Garrahan, and R. Gutiérrez, Glassy dynamics due to a trajectory phase transition in dissipative Rydberg gases, *Phys. Rev. A* **98**, 021804 (2018).
- [84] D. Gribben, I. Lesanovsky, and R. Gutiérrez, Quench dynamics of a dissipative Rydberg gas in the classical and quantum regimes, *Phys. Rev. A* **97**, 011603 (2018).
- [85] C. Ates, B. Olmos, J. P. Garrahan, and I. Lesanovsky, Dynamical phases and intermittency of the dissipative quantum Ising model, *Phys. Rev. A* **85**, 043620 (2012).
- [86] I. Lesanovsky, M. van Horssen, M. Guță, and J. P. Garrahan, Characterization of Dynamical Phase Transitions in Quantum Jump Trajectories Beyond the Properties of the Stationary State, *Phys. Rev. Lett.* **110**, 150401 (2013).
- [87] B. Olmos, I. Lesanovsky, and J. P. Garrahan, Out-of-equilibrium evolution of kinetically constrained many-body quantum systems under purely dissipative dynamics, *Phys. Rev. E* **90**, 042147 (2014).
- [88] M. van Horssen, E. Levi, and J. P. Garrahan, Dynamics of many-body localization in a translation-invariant quantum glass model, *Phys. Rev. B* **92**, 100305 (2015).
- [89] Z. Lan, M. van Horssen, S. Powell, and J. P. Garrahan, Quantum Slow Relaxation and Metastability due to Dynamical Constraints, *Phys. Rev. Lett.* **121**, 040603 (2018).
- [90] D. C. Rose, K. Macieszczak, I. Lesanovsky, and J. P. Garrahan, Hierarchical classical metastability in an open quantum East model, *Phys. Rev. E* **105**, 044121 (2022).
- [91] R. J. Valencia-Tortora, N. Pancotti, and J. Marino, Kinetically Constrained Quantum Dynamics in Superconducting Circuits, *PRX Quantum* **3**, 020346 (2022).
- [92] K. Yamamoto and R. Hamazaki, Measurement-induced crossover of quantum jump statistics in postselection-free many-body dynamics, [arXiv:2503.02418](https://arxiv.org/abs/2503.02418) (2025).
- [93] M. Cech, M. Cea, M. C. Bañuls, I. Lesanovsky, and F. Carollo, Space-Time Correlations in Monitored Kinetically Constrained Discrete-Time Quantum Dynamics, *Phys. Rev. Lett.* **134**, 230403 (2025).
- [94] L. Causer, M. C. Bañuls, and J. P. Garrahan, Dynamical heterogeneity and large deviations in the open quantum East glass model from tensor networks, *Phys. Rev. B* **111**, L060303 (2025).
- [95] P. Strasberg, G. Schaller, T. Brandes, and M. Esposito, Quantum and Information Thermodynamics: A Unifying Framework Based on Repeated Interactions, *Phys. Rev. X* **7**, 021003 (2017).
- [96] M. Cattaneo, G. L. Giorgi, R. Zambrini, and S. Maniscalco, A brief journey through collision models for multipartite open quantum dynamics, *Open Syst. Inf. Dyn.* **29**, 2250015 (2022).
- [97] F. Ciccarello, S. Lorenzo, V. Giovannetti, and G. M. Palma, Quantum collision models: open system dynamics from repeated interactions, *Phys. Rep.* **954**, 1 (2022).
- [98] K. Kraus, A. Böhm, J. Dollard, and W. Wootters, *States, Effects, and Operations: Fundamental Notions of Quantum Theory*, Lecture Notes in Physics (Springer Berlin Heidelberg, 1983).
- [99] Note that, in the continuous-time limit $\Delta t \rightarrow 0$, the dynamics can be described by a Lindblad master equation with Hamiltonian $H_S = \Omega \sum_{i=1}^L \sigma_i^x + V \sum_{i=1}^{L-1} n_i n_{i+1}$ and jump operators $J_i = \sqrt{\gamma} P_i$.
- [100] See Supplemental Material, which further contains Refs. [101–116], for details.
- [101] G. E. Fux, D. Kilda, B. W. Lovett, and J. Keeling, Tensor network simulation of chains of non-Markovian open quantum systems, *Phys. Rev. Research* **5**, 033078 (2023).
- [102] M. Fishman, S. R. White, and E. M. Stoudenmire, The ITensor Software Library for Tensor Network Calculations, *SciPost Phys. Codebases*, 4 (2022).
- [103] G. Vidal, Efficient Classical Simulation of Slightly Entangled Quantum Computations, *Phys. Rev. Lett.* **91**, 147902 (2003).
- [104] G. Vidal, Efficient Simulation of One-Dimensional Quantum Many-Body Systems, *Phys. Rev. Lett.* **93**, 040502 (2004).
- [105] S. Paeckel, T. Köhler, A. Swoboda, S. R. Manmana, U. Schollwöck, and C. Hubig, Time-evolution methods for matrix-product states, *Ann. Phys.* **411**, 167998 (2019).
- [106] N. Hatano and M. Suzuki, Finding exponential product formulas of higher orders, in *Quantum Annealing and Other Optimization Methods*, edited by A. Das and B. K. Chakrabarti (Springer Berlin Heidelberg, 2005) pp. 37–68.
- [107] A. J. Ferris and G. Vidal, Perfect sampling with unitary tensor networks, *Phys. Rev. B* **85**, 165146 (2012), 1201.3974.
- [108] G. T. Landi, Patterns in the jump-channel statistics of open quantum systems, [arXiv:2305.07957](https://arxiv.org/abs/2305.07957) (2023).
- [109] E. Gillman, F. Carollo, and I. Lesanovsky, Numerical simulation of critical dissipative non-equilibrium quantum systems with an absorbing state, *New J. Phys.* **21**, 093064 (2019).
- [110] M. Frías-Pérez and M. C. Bañuls, Light cone tensor network and time evolution, *Phys. Rev. B* **106**, 115117 (2022).
- [111] S. Katira, J. P. Garrahan, and K. K. Mandadapu, Solvation in Space-time: Pretransition Effects in Trajectory Space, *Phys. Rev. Lett.* **120**, 260602 (2018).
- [112] K. Klobas, C. De Fazio, and J. P. Garrahan, Exact pretransition effects in kinetically constrained circuits: Dynamical fluctuations in the Floquet-East model, *Phys. Rev. E* **110**, L022101 (2024).
- [113] C. De Fazio, J. P. Garrahan, and K. Klobas, Exact results on the dynamics of the stochastic Floquet-East model, *J. Phys. A: Math. Theor.* **57**, 505002 (2024).
- [114] I. Lesanovsky and H. Katsura, Interacting Fibonacci anyons in a Rydberg gas, *Phys. Rev. A* **86**, 041601 (2012).
- [115] C. J. Turner, A. A. Michailidis, D. A. Abanin, M. Serbyn, and Z. Papić, Quantum scarred eigenstates in a Rydberg atom chain: Entanglement, breakdown of thermalization, and stability to perturbations, *Phys. Rev. B* **98**, 155134 (2018).
- [116] S. Wald, L. H. Yao, T. Platini, C. Hooley, and F. Carollo, Stochastic resetting in discrete-time quantum dynamics: steady states and correlations in few-qubit systems, *Quantum* **9**, 1742 (2025).
- [117] M. P. A. Fisher, V. Khemani, A. Nahum, and S. Vijay, Random Quantum Circuits, *Annu. Rev. Condens. Matter Phys.* **14**, 335 (2023).
- [118] G. Passarelli, X. Turkeshi, A. Russomanno, P. Lucignano, M. Schirò, and R. Fazio, Many-Body Dynamics in Monitored Atomic Gases without Postselection Barrier, *Phys. Rev. Lett.* **132**, 163401 (2024).

- [119] S. J. Garratt and E. Altman, Probing Postmeasurement Entanglement without Postselection, *PRX Quantum* **5**, 030311 (2024).
- [120] J. Li, R. L. Jack, B. Bertini, and J. P. Garrahan, Efficient post-selection in light cone correlations of monitored quantum circuits, *Phys. Rev. B* **111**, 024309 (2025).
- [121] D. Chandler, Interfaces and the driving force of hydrophobic assembly, *Nature* **437**, 640 (2005).
- [122] A. P. Willard and D. Chandler, The Role of Solvent Fluctuations in Hydrophobic Assembly, *J. Phys. Chem. B* **112**, 6187 (2008).
- [123] K. Lum, D. Chandler, and J. D. Weeks, Hydrophobicity at Small and Large Length Scales, *J. Phys. Chem. B* **103**, 4570 (1999).
- [124] M. Cech, C. De Fazio, M. Cea, M. C. Bañuls, I. Lesanovsky, and F. Carollo, Data and code for “Revealing emergent phenomena by analyzing large-scale space-time records of monitored quantum systems” (2025).

SUPPLEMENTAL MATERIAL

Revealing emergent many-body phenomena by analyzing large-scale space-time records of monitored quantum systems

Marcel Cech,¹ Cecilia De Fazio,¹ María Cea,^{2,3} Mari Carmen Bañuls,^{2,3} Igor Lesanovsky,^{1,4} and Federico Carollo⁵

¹*Institut für Theoretische Physik and Center for Integrated Quantum Science and Technology, Universität Tübingen, Auf der Morgenstelle 14, 72076 Tübingen, Germany*

²*Max-Planck-Institut für Quantenoptik, Hans-Kopfermann-Str. 1, D-85748 Garching, Germany*

³*Munich Center for Quantum Science and Technology (MCQST), Schellingstr. 4, D-80799 München, Germany*

⁴*School of Physics and Astronomy and Centre for the Mathematics and Theoretical Physics of Quantum Non-Equilibrium Systems,*

The University of Nottingham, Nottingham, NG7 2RD, United Kingdom

⁵*Centre for Fluid and Complex Systems, Coventry University, Coventry, CV1 2TT, United Kingdom*

I. TENSOR NETWORK METHODS

In this section, we discuss the tensor network methods employed to generate the data analyzed in the main text. In Sec. IA, we focus on simulations of the stochastic dynamics in terms of discrete-time quantum-jump Monte Carlo (QJMC) trajectories, which can be obtained by sampling measurement outcomes on the ancillas. In Sec. IB, we present the appropriately conditioned average state evolution that allows us to compute quantities such as the probability of inactive space-time clusters and the autocorrelation functions. Furthermore, in Tab. S1, we provide a schematic summary of the methods and parameters used for each figure in the main text. For both instances, we explicitly include the ancillas in our tensor network ansatz (see also Ref. [101] for a similar approach). We further note that we utilize the open-source ITensors.jl-library [102] to implement common tensor network routines like contractions and singular-value decompositions (SVDs).

TABLE S1. **Tensor network specifications.** For the results presented in the main manuscript, we specify the method alongside the maximal bond dimension χ or the SVD cutoff ϵ , which control the accuracy of the simulation. List of abbreviations: MPS = matrix product state, QJMC = quantum jump Monte-Carlo (see Sec. IA), MPO = matrix product operator, bw-evo = backward evolution, tw-evo = evolution in two ways (see Sec. IB).

Figure	Panel	Description	Method	maximal bond dimension χ	SVD cutoff ϵ
1	(c,d)	stochastic realization	MPS-QJMC	-	10^{-10}
2	(a)	empirical $p_{\ell \times \tau}$	MPS-QJMC	-	10^{-8}
	(a-c)	$p_{\ell \times \tau}$	MPO bw-evo	64	-
3	(a)	$p_{\ell \times \tau}$ & $p_{\ell \times \tau, \delta_i}$	MPO bw-evo	64	-
	(b)	$p_{\ell \times \tau, \delta_t}$	MPO tw-evo	64	-
		$p_{\ell \times \tau}$	MPO bw-evo	64	-
4	-	empirical $c_{\delta_t}^{(i)}$	MPS-QJMC	-	10^{-8}
		$c_{\delta_t}^{(i)}$	MPO tw-evo	64	-

A. Discrete-time quantum-jump Monte-Carlo simulation

Simulating the stochastic dynamics requires us to follow the three-step procedure depicted in Fig. 1(a). We here report a detailed description of how these steps are implemented with tensor network.

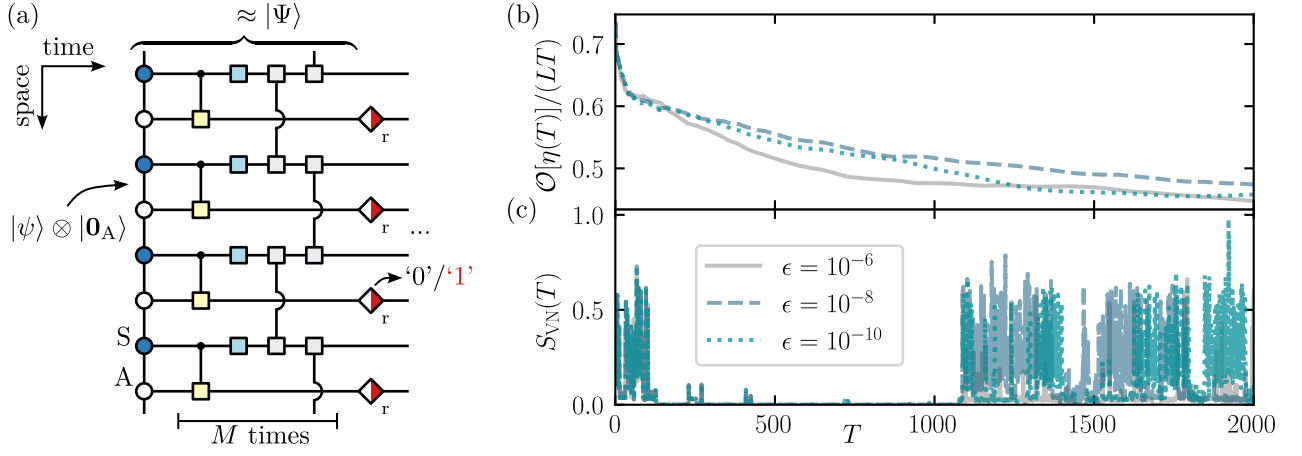


FIG. S1. **Tensor network simulation of stochastic dynamics.** (a) Tensor network diagram implementing the discrete-time quantum-jump Monte-Carlo (QJMC) evolution. The blue and white circles in the MPS diagram represent the tensors for the system and ancilla qubits, respectively. Squares denote unitary gates [see Eq. (S2)], while two-colored diamonds represent the projective measurement of ancillas in the computational basis $\{|0_A\rangle, |1_A\rangle\}$ combined with the subsequent resetting to $|0_A\rangle$. (b,c) Comparison of stochastic realizations simulated with different SVD cutoffs ϵ . We compare the average number of the number of ‘1’ ancilla measurement outcomes over time [see Eq. (S3)] and the half-chain entanglement entropy $S_{VN}(T)$ [see Eq. (S4)]. Here, $L = 60$, $\Omega\Delta t = 1.25$, $V = 5.875\Omega$, $\gamma = 3\Omega$ and $M = 10$.

At a given time t , the state of the system is described by the vector $|\psi\rangle$. The total system-ancillas state thus reads $|\psi\rangle \otimes |\mathbf{0}_A\rangle$ and, under the subsequent unitary evolution, it becomes $|\Psi\rangle = U(|\psi\rangle \otimes |\mathbf{0}_A\rangle)$ [see Eq. (1)]. Assuming that one has an accurate Matrix Product State (MPS) representation of $|\psi\rangle \otimes |\mathbf{0}_A\rangle$, the unitary evolution, represented by step (i) in Fig. 1(a), can be implemented using the time-evolution block decomposition (TEBD) algorithm [103–105]. To this end, we approximate the unitary U using a first-order Trotter decomposition [106]

$$U = e^{-iH_{CM}\Delta t} = \left(e^{-iH_{CM}\Delta t/M} \right)^M \approx \left(\underbrace{e^{-i\frac{V\Delta t}{M} \sum n_i n_{i+1}} \cdot e^{-i\frac{\Omega\Delta t}{M} \sum \sigma_i^x}}_{\text{system only}} \cdot \underbrace{e^{-i\frac{\gamma_0\Delta t}{M} \sum P_i \otimes \sigma_i^x}}_{\text{system-ancilla int.}} \right)^M, \quad (\text{S1})$$

with $M = 10$. The tensor network diagram in Fig. S1(a) shows this decomposition in terms of the gates:

$$\begin{array}{c} \text{---} \\ | \\ \text{---} \\ \text{---} \\ | \\ \text{---} \end{array} = e^{-i\frac{\gamma_0\Delta t}{M} P \otimes \sigma^x}, \quad \begin{array}{c} \text{---} \\ | \\ \text{---} \\ \text{---} \\ | \\ \text{---} \end{array} = e^{-i\frac{\Omega\Delta t}{M} \sigma^x}, \quad \begin{array}{c} \text{---} \\ | \\ \text{---} \\ \text{---} \\ | \\ \text{---} \end{array} = e^{-i\frac{V\Delta t}{M} n \otimes n}, \quad (\text{S2})$$

where operators on the left-hand side of the tensor product act on the upper qubit in the graphical representation. Once an accurate approximation of the state $|\Psi\rangle$ has been obtained, we implement the local ancilla measurements according to Born’s rule, corresponding to step (ii) in Fig. 1(a). This Monte-Carlo sampling procedure, known in the context of MPS as direct (perfect) sampling algorithm [107], returns (upon normalization) the post-measurement system-ancilla state $|\psi'\rangle \otimes |\mathbf{k}_A\rangle$, where $\mathbf{k} = (k_1, \dots, k_L)$ denotes the ancillas’ outcome and $|\psi'\rangle = K_{\mathbf{k}} |\psi\rangle / \|K_{\mathbf{k}} |\psi\rangle\|$ is the system’s state. This procedure, combined with resetting the ancillas to the reference state $|\mathbf{0}_A\rangle$, is implemented through the local, non-unitary gate \blacklozenge_r as shown in Fig. S1(a), and completes step (iii) in Fig. 1(a).

To obtain individual realizations of the stochastic dynamics, e.g., the one shown in Fig. 1(c,d), we initialize the system in $|\psi_0\rangle = |\mathbf{0}_S\rangle$ and iterate the above approach T times. We can control the trade-off between accuracy and computational complexity by setting a lower limit, or cutoff, ϵ on the Schmidt coefficients that are taken into account, when evolving the MPS according to Fig. S1(a). We generate the random numbers required for the direct sampling using a fixed seed. As it can be seen below, this enables us to analyze the influence of the truncation more effectively, while not giving up the stochastic nature of the ancilla outcomes.

We now focus on two quantities: an observable on the space-time records of ancilla measurement outcomes and the entanglement entropy. For the first, we consider the average activity introduced in Ref. [93], which quantifies the density of ‘1’ ancilla measurement outcomes within a space-time region of size $L \times T$, namely

$$\frac{1}{LT} \mathcal{O}[\eta(T)] = \frac{1}{LT} \sum_{t=1}^T \sum_{i=1}^L k_i(t). \quad (\text{S3})$$

The instantaneous half-chain entanglement entropy at stroboscopic times T is defined as

$$S_{\text{VN}}(T) = -\text{Tr}\{\rho_T^{\text{red.}} \log(\rho_T^{\text{red.}})\}, \quad (\text{S4})$$

where we introduced the reduced density matrix:

$$\rho_T^{\text{red.}} = \text{Tr}_{(i>L/2)}\{|\psi_T\rangle\langle\psi_T|\}. \quad (\text{S5})$$

Fig. S1(b,c) show the two quantities as functions of time. Apart from an overall qualitative agreement, we observe that, after $T \approx 100$ time steps, both the average activity and the instantaneous half-chain entanglement entropy become sensitive to the cutoff ϵ . In particular, we notice that the quantities do not converge in a uniform way upon increasing the accuracy with smaller values of ϵ . However, the instantaneous entanglement entropy does not significantly increase with smaller values of ϵ indicating that states of the stochastic realization are overall well approximated. Discrepancies between the different curves are due to the fact that even a slight modification in the calculation of the state affects the probability of observing a certain set of ancilla measurement outcomes \mathbf{k} , i.e., $\pi(\mathbf{k}) = \langle\Psi|(\mathbb{1} \otimes |\mathbf{k}_A\rangle\langle\mathbf{k}_A|)|\Psi\rangle$. Over a long time, this can eventually alter the outcome of a single ancilla measurement, and thereby completely change its subsequent evolution.

However, for sufficiently small values of ϵ and large enough sample sizes, we do not expect this to affect the behavior of empirical quantities such as the probability of inactive clusters and the temporal autocorrelation function. In practice, we find that setting the cutoff to $\epsilon = 10^{-8}$ yields accurate results for Figs. 2 and 4 at relatively low computational cost.

B. Ensemble averages from average state calculations

As a next step, we describe the average state calculations, which allow us to compute the probabilities of inactive clusters and the autocorrelation function as an ensemble average at stationarity. These quantities can be understood as observables in the space of quantum trajectories, as determined by ancillary measurement outcomes. This means that their long-time averages can be computed via an appropriately conditioned time evolution of the stationary state [108], here given by the fully mixed state $\rho_{\text{ss}} = \mathbb{1}/2^L$ [93].

Concretely, the condition to encounter an inactive region of length ℓ at a given time of the dynamics can be implemented through the transfer operator $T_\ell[\rho]$. This operator describes the average state evolution selecting only those trajectories in which at least ℓ central ancilla outcomes are ‘0’, namely

$$T_\ell[\rho] = \text{Tr}_A\{\mathcal{P}_\ell U(\rho \otimes |0_A\rangle\langle 0_A|)U^\dagger \mathcal{P}_\ell\}, \quad (\text{S6})$$

where $\mathcal{P}_\ell = |0_A\rangle\langle 0_A|^{\otimes \ell}$ is a local projector onto ℓ central sites of the ancillas in the zero state. Through this quantity, we can define the probability $p_{\ell \times \tau}$ of an $\ell \times \tau$ -sized inactive cluster as

$$p_{\ell \times \tau} = \text{Tr}\{(T_\ell)^\tau[\rho_{\text{ss}}]\}, \quad (\text{S7})$$

where the required conditioned evolution is implemented by repeated application of the transfer operator $T_\ell[\rho]$ over a time interval τ . Similarly, we can also construct the conditioned evolution targeting the autocorrelation function [cf. Eq. (5) and Ref. [93]] and the probability of two identical inactive cluster separated in time or space, i.e.,

$$p_{\ell \times \tau, \delta_t} = \text{Tr}\{(T_\ell)^\tau \circ \mathcal{E}^{\delta_t} \circ (T_\ell)^\tau[\rho_{\text{ss}}]\}, \quad (\text{S8})$$

$$p_{\ell \times \tau, \delta_i} = \text{Tr}\{(T_{\ell, \delta_i})^\tau[\rho_{\text{ss}}]\}, \quad (\text{S9})$$

Here, the unconditioned evolution under $\mathcal{E}[\rho] = \text{Tr}_A\{U(\rho \otimes |0_A\rangle\langle 0_A|)U^\dagger\}$ (the accordingly conditioned transfer operator T_{ℓ, δ_i}) marginalizes over the δ_t (δ_i) ancilla measurement outcomes between the two $\ell \times \tau$ -sized inactive regions.

Taking the probability in Eq. (S7) and the autocorrelation function in Eq. (5) as an example, we show their corresponding tensor network representations in panels (a) and (b) of Fig. S2, respectively. In both panels, the dynamics is implemented in a folded space, where two layers similar to the one in Fig. S1(a) are combined to represent the evolution in the space of density matrices. Representing the system-ancilla state as Matrix Product Operator (MPO), the unitary evolution, shown as connected gray gates in Fig. S2, can still be obtained via the

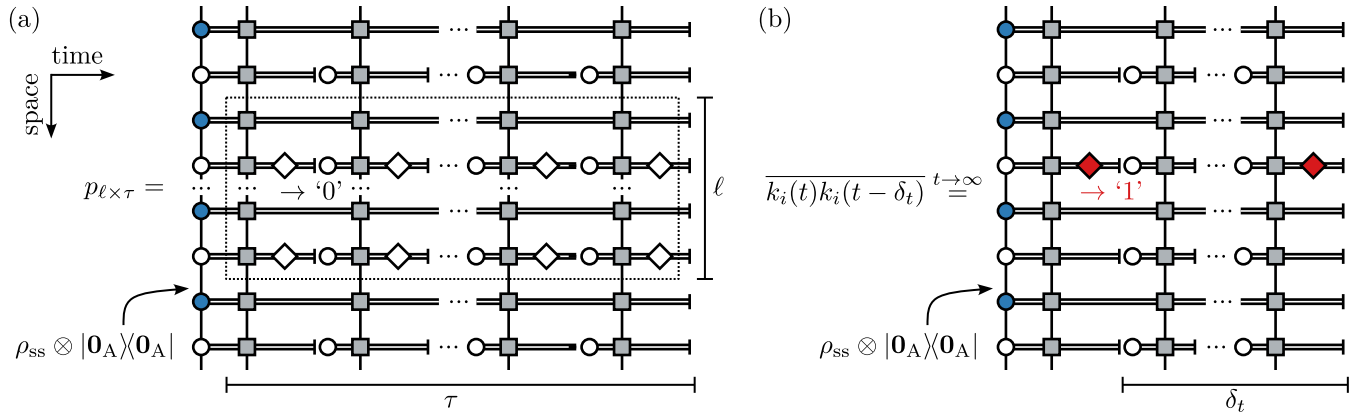


FIG. S2. **Tensor network diagrams for average state calculations.** We show the tensor network diagrams corresponding to (a) the probability $p_{\ell \times \tau}$ of an inactive space-time cluster as given by Eqs. (S6,S7) and (b) the two-point ancilla expectation value $\overline{k_i(t)k_i(t - \delta_t)}$ entering the autocorrelation $c_{\delta_t}^{(i)}$ in Eq. (5). Following the example of Eq. (S6), this incorporates the repeated, joined unitary evolution [gray gates] and appropriate projections on the ancillary degrees of freedom [white and red diamond for ‘0’ and ‘1’, respectively]. Note that we use double lines to distinguish the MPO evolution in the space of density matrices from the MPS evolution of a pure state in Fig. S1(a).

Trotter-Suzuki decomposition in analogy with the procedure outlined in the previous section. Here, we set a maximum bond dimension χ in the SVDs of the TEBD algorithm. This step is followed by applying single-site projectors on state $|0_A\rangle$ or $|1_A\rangle$ [see \diamond or \blacklozenge in Fig. S2], when calculating the probability of an inactive cluster or the autocorrelation function in Eq. (5), respectively. Finally, we trace over all ancillas before resetting them to the state $|0_A\rangle$ [see \circ in Fig. S2] to prepare for the next time step.

Let us also remark that the tensor network diagram representation does not stipulate that contractions must be performed in the forward direction, as described above. Taking inspiration from Refs. [109, 110], we can use the backward or two-way evolution to reduce the computational cost as measured by the required bond dimension and the number of individual contractions to obtain the same level of accuracy (see Tab. S1 for the individual specifications). Furthermore, to avoid instabilities due to small numerical values, we always compute and store the multiplicative increment, e.g., $p_{\ell \times (\tau+1)}/p_{\ell \times \tau}$, and only later access the full quantity as cumulative product.

Finally, we verify that the chosen bond dimension of $\chi = 64$ is sufficient to capture the quantities presented in Figs. 2-4. We therefore repeat all simulations with both decreased and increased accuracy, and display the resulting probabilities or the autocorrelation function over time in Fig. S3. Here, we observe that simulations with a bond dimension of $\chi = 32$ show minor differences, while the agreement between $\chi = 64$ and $\chi = 128$ signals the convergence of the results.

II. FURTHER DISCUSSION ON INACTIVE CLUSTERS

In this section, we provide further discussions of the inactive clusters and their corresponding free energies. In particular, we compare the associated interface tensions $\Delta_\ell F_{\ell \times \tau}$ and $\Delta_\tau F_{\ell \times \tau}$ depicted in Fig. S4(a), which represent the free-energy cost of extending the cluster in either space or time.

We start by recalling the definition of the dynamical free energy in Eq. (3), which is expressed in terms of the probability of finding an inactive region of size $\ell \times \tau$. This probability can be computed using the procedure outlined in the previous section. Taking inspiration from Refs. [111–113], we study the scaling behavior of the dynamical free energies by making the following ansatz

$$F_{\ell \times \tau} = \alpha_{\ell, \tau} \ell \tau + \beta_\tau \tau + \beta_\ell \ell + \text{const.} \quad (\text{S10})$$

The coefficients α and β are evaluated numerically and control the contributions of the area $\ell \tau$, and the perimeter $\ell + \tau$ of the considered space-time region, respectively. Note that these coefficients may potentially depend on ℓ and

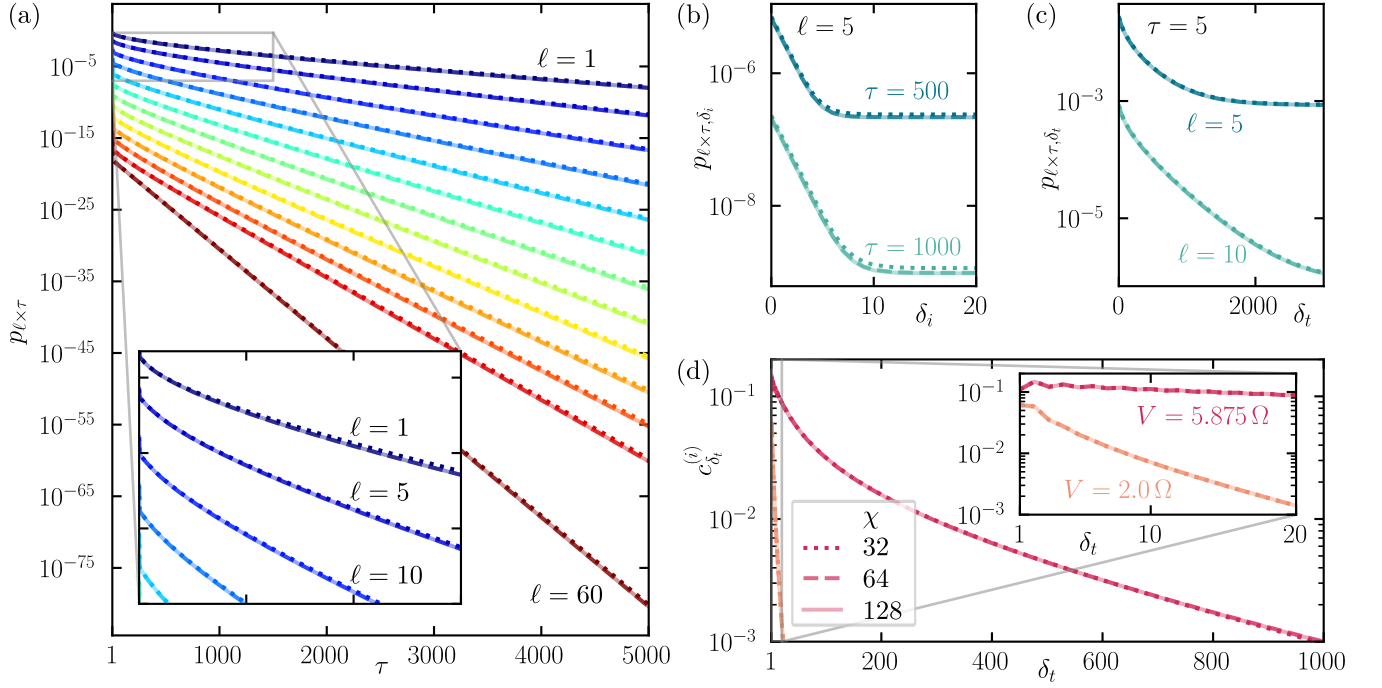


FIG. S3. **Convergence checks of average state calculations.** We compare results obtained for different bond dimensions $\chi = 32, 64, 128$ as dotted, dashed and solid lines with fading opacity. (a) Probability $p_{\ell \times \tau}$ of inactive space-time regions with fixed spatial size $\ell \in \{1, 5, 10, \dots, 60\}$ as a function of the temporal extension τ entering Figs. 2 and 3. (b,c) Probability $p_{\ell \times \tau, \delta_i}$ and $p_{\ell \times \tau, \delta_t}$ of inactive regions separated by δ_i δ_t considered in Fig. 3. (c) Autocorrelation function for the ideal case as a function of the time difference δ_t shown in Fig. 4. If not stated otherwise, we consider $L = 60$, $\Omega \Delta t = 1.25$, $V = 5.875 \Omega$, $\gamma = 3 \Omega$ and $M = 10$.

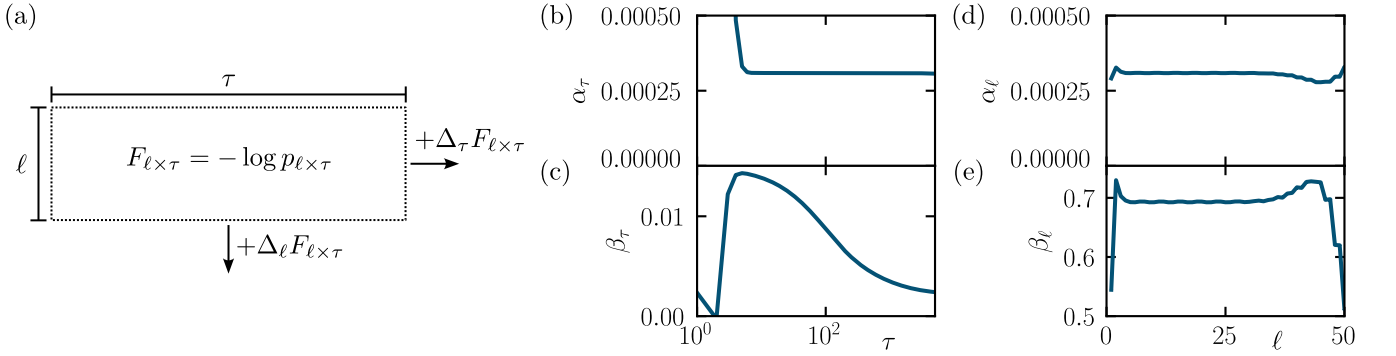


FIG. S4. **Inactive space-time cluster.** (a) Graphical representation of the spatial and temporal interface tensions of inactive cluster. (b,c) Numerical coefficients α_τ and β_τ as extracted from linear fitting of $\Delta_\tau F_{\ell \times \tau}$ in Eq. (4) within the range of $10 \leq \ell \leq 40$. (d,e) Numerical coefficients α_ℓ and β_ℓ as extracted from linear fitting of $\Delta_\ell F_{\ell \times \tau}$ according to Eq. (S11) in the interval specified by $2000 \leq \tau \leq 3000$. Here, $L = 60$, $\Omega \Delta t = 1.25$, $\gamma = 3 \Omega$, $V = 5.875 \Omega$ with $M = 10$ and $\chi = 64$.

τ , as indicated by their corresponding subscripts.

Eq. (S10) is consistent with the ansatz for the temporal interface tension in Eq. (4), whose numerical parameters are shown in the central panels of Fig. S4. We notice that the crossover from (I) to (II) observed in Fig. 2(c) occurs due to the decrease of α_τ and a simultaneous increase of β_τ . On the other hand, we find that β_τ then decreases again, making it, in principle, easier to maintain a inactive space-time region while reestablishing a more dominant role for the area scaling with α_τ , as seen in the crossover from (II) to (III) in Fig. 2(c).

Similarly, an ansatz can be formulated for the spatial interface tension, defined as the increment in the dynamical

free energy obtained by extending the inactive space-time cluster by a unit of space, which reads

$$\Delta_\ell F_{\ell \times \tau} = F_{(\ell+1) \times \tau} - F_{\ell \times \tau} = \alpha_\ell \tau + \beta_\ell. \quad (\text{S11})$$

Numerical values of the parameters α_ℓ and β_ℓ are shown in Fig. S4, right panels. We observe that the inferred values of α_ℓ in panel (d) agree well with those of α_τ in panel (b) over a large range of cluster sizes, further confirming the applicability of the ansatz in Eq. (S10). Furthermore, we note that the perimeter-related contribution given by β_ℓ in panel (e) is significantly larger than the counterpart in time shown in panel (c). This indicates that it is more favorable to extend clusters in time rather than in space. On the one hand, this difference is already reflected in the clusters with long temporal extents observed in Fig. 1(d). On the other hand, it explains why correlations persist longer in time than in space [cf. Fig. 3]. Finally, we note that the deviation from approximately constant values of α_ℓ and β_ℓ for $\ell \gtrsim 40$ indicates the presence of boundary effects.

III. TUNEABLE DYNAMICAL PHASE COEXISTENCE

In this section, we investigate the dependence of the dynamical phase coexistence, as seen in Fig. 1(c,d), on the atom-atom interaction strength V [cf. Eq. (2)].

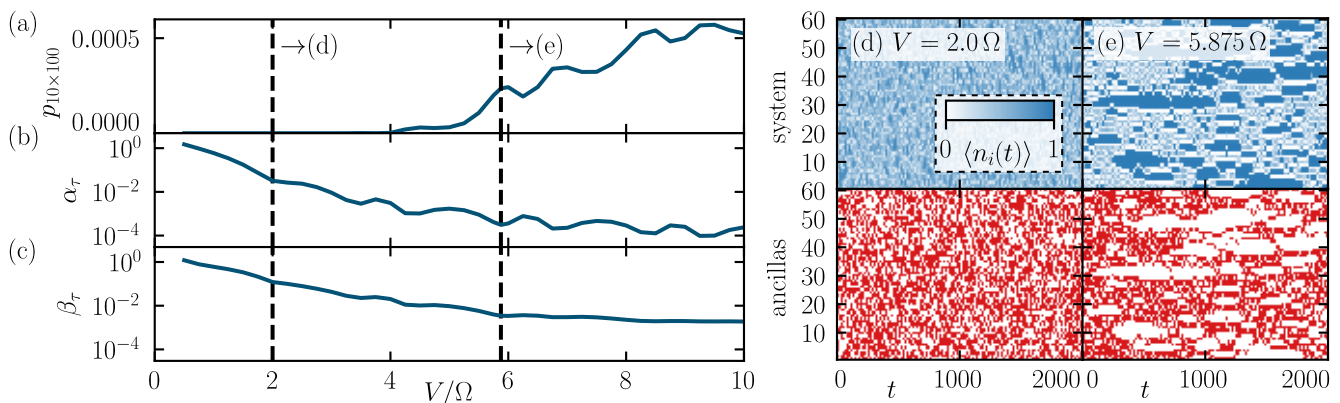


FIG. S5. **Tuneable dynamical phase coexistence.** (a) Probability of 10×100 -sized inactive space-time regions for atom-atom interaction strengths V . (b,c) Area- and perimeter-scaling coefficients α_τ and β_τ . We show the coefficients extracted from fitting the temporal interface tension, $\Delta_\tau F_{\ell \times \tau}$, at $\ell \in \{10, 20, 30, 40\}$ and $\tau = 1000$ according to Eq. (4). (d,e) Stochastic realizations and corresponding space-time resolved quantum trajectory for $V = 2\Omega$ and $V = 5.875\Omega$ [see vertical dashed lines in panels (a-c)]. We consider $L = 60$, $\gamma = 3\Omega$, $\Omega\Delta t = 1.25$, $M = 10$ with $\chi = 64$ (a-c) or $\epsilon = 10^{-10}$ (d,e), respectively.

Figure S5(a) shows how the probability of finding $\ell \times \tau$ -sized inactive cluster, i.e., for $\ell = 10$ and $\tau = 100$, varies with the interaction strength V . We observe that this probability is distinguishable from zero for $V \gtrsim 4\Omega$, where Ω is the Rabi frequency. We observe that this probability generally increases with V , while displaying an oscillatory behavior. To understand this behavior, we need to consider two contributions. On the one hand, the dynamical phase coexistence becomes more pronounced as V increases, factually freezing the dynamics of adjacent atoms in the excited state $|1_S\rangle$ for $V \rightarrow \infty$ [114, 115]. On the other hand, the superimposed oscillatory behavior can be understood by recalling that the discrete-time quantum dynamics can display resonances, which would not be present in the continuous-time generator, i.e., H_{CM} in Eq. (2) [116]. We note that the increase in the probability in panel (a) is a directly connected to the decrease of several orders of magnitude in the coefficients α_τ and β_τ in panels (b,c).

Finally, we show two stochastic realizations alongside their respective space-time resolved quantum trajectories in Figs. S5(d,e). For the chosen values of $V = 2\Omega$ and $V = 5.875\Omega$, only the trajectory for $V = 5.875\Omega$ displays a large-scale coexistence of inactive and active space-time regions, thus confirming the expectation from panels (a-c).

IV. DETAILS ON EMPIRICAL QUANTITIES OF QUANTUM TRAJECTORIES

In this section, we discuss the details on evaluating the simulated trajectories to extract empirically the probabilities and the autocorrelation function shown as symbols in Fig. 2 and Fig. 4, respectively. In particular, we discuss the influence of averaging over both space and time in the presence of experimental imperfections.

Following the approach outlined in Ref. [93], here applied to larger system sizes, we employ the concept of time-integrated observables on individual trajectories to estimate the probabilities of inactive regions and the autocorrelation function in two stages. In particular, we expect that the long-time average accesses the stationary behavior of these quantities. After averaging over space and time, we calculate the mean of a few simulated trajectories to determine their empirical value. We then estimate the statistical uncertainty to be twice the standard error. By restricting ourselves to ancilla outcomes at least five sites away from the boundaries, we avoid boundary effects while simultaneously increasing statistical accuracy as compared to evaluating a single ancilla site i . As demonstrated in Fig. 2(a), 20 quantum trajectories with 100 000 time steps each are sufficient to capture the probabilities of inactive regions well down to 10^{-4} .

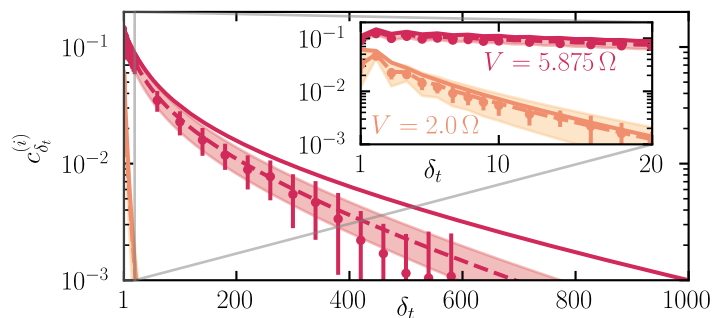


FIG. S6. **Alternative view on the autocorrelation function.** Similar to Fig. 4, we compare the ideal dynamics (solid lines) to observations made under experimental imperfections. For the latter, we consider ten disorder sets of disordered couplings, i.e., V and γ locally varied within a range of up to $\pm\Omega$. For all of them, we simulate both a quantum trajectory over 100 000 time steps (symbols, incorporating also $p_{\text{err}} = 2\%$ of bit-flip errors) and appropriately conditioned average state calculations (dashed lines with shaded regions indicating the statistical uncertainties). Note that in contrast to Fig. 4, we only evaluate the most central ancilla outcomes. Throughout, we set $L = 60$, $\gamma = 3\Omega$, $\Omega\Delta t = 1.25$, $M = 10$ with $\chi = 64$ (average state calculations) and $\epsilon = 10^{-8}$ (quantum trajectories), respectively.

To highlight especially the effect of the spatial average in this approach, we revisit the autocorrelation function in the presence of experimental imperfections. In contrast to Fig. 4, where the square symbols are extracted from a large number of ancilla measurement outcomes in the bulk, we now focus only on the central ones. In Fig. S6, we then observe two important aspects of this modification. Firstly, as expected, we notice an increase in the statistical uncertainty. Furthermore, the autocorrelation function with experimental imperfections, which takes into account only the most central ancillas, decreases slightly faster for $V = 5.875\Omega$ than was previously observed in Fig. 4. In fact, the local maximum of the probability for a mesoscopic inactive cluster, as observed around $V = 5.875\Omega$ in Fig. S5(a), suggests that changes to the parameters of the Hamiltonian in Eq. (2) would have a diminishing impact on the signatures of the dynamical phase coexistence. However, when we compare Fig. 4 with Fig. S6, we can see that incorporating ancilla measurement outcomes over a larger spatial region in the quantum trajectory effectively increases the likelihood of finding long-lived correlations that resemble the ones in the ideal case.